DRAFT VERSION OCTOBER 11, 2021
Preprint typeset using LaTeX style emulateapj v. 12/16/11

LONG-LIVED ECCENTRIC MODES IN CIRCUMBINARY DISKS

DIEGO J. MUÑOZ AND YORAM LITHWICK
Center for Interdisciplinary Exploration and Research in Astrophysics, Physics and Astronomy, Northwestern University, Evanston, IL 60208, USA

Draft version October 11, 2021

ABSTRACT

Hydrodynamical simulations show that circumbinary disks become eccentric, even when the binary is circular. Here we demonstrate that, in steady state, the disk's eccentricity behaves as a long-lived free mode trapped by turning points that naturally arise from a continuously truncated density profile. Consequently, both the disk's precession rate and eccentricity profile may be calculated via the simple linear theory for perturbed pressure-supported disks. By formulating and solving the linear theory we find that (i) surprisingly, the precession rate is roughly determined by the binary's quadrupole, even when the quadrupole is very weak relative to pressure; (ii) the eccentricity profile is largest near the inner edge of the disk, and falls exponentially outwards; and (iii) the results from linear theory indeed agree with what is found in simulations. Understanding the development of eccentric modes in circumbinary disks is a crucial first step for understanding the long term (secular) exchange of eccentricity, angular momentum and mass between the binary and the gas. Potential applications include the search for a characteristic kinematic signature in disks around candidate binaries and precession-induced modulation of accretion over long timescales.

Keywords: accretion, accretion disks – binaries: general – stars: pre-main sequence

1. INTRODUCTION

Gas eccentricity is expected to grow in disks inside and around binaries (e.g. Lubow 1991; Whitehurst 1994; Paardekooper et al. 2008; Kley et al. 2008). In particular, two-dimensional hydrodynamical simulations of circumbinary disks (CBDs) have consistently shown significant eccentricities (~ 0.3), even when the binary is circular (MacFadyen & Milosavljević 2008; Miranda et al. 2017; Thun et al. 2017). Typically, the eccentricity is large near the circumbinary "cavity" and steeply declines outward. This overall behavior has been seen also in three-dimensional magneto-hydrodynamics simulations (Shi et al. 2012), which suggests that the growth of eccentricity is a robust property of disks around accreting binaries.

The mechanisms for eccentricity growth are thought to be either resonant excitation (Lubow 1991; Ogilvie 2007) or periodic "pumping" via oblique spiral shocks (Shi et al. 2012). The mechanisms for eccentricity damping are less constrained, although viscous damping (Goodchild & Ogilvie 2006), orbit-crossing (Ogilvie 2001; Statler 2001), or combinations thereof are the likely processes behind eccentricity saturation. The nearly steady eccentricity profiles of some numerical simulations (Miranda et al. 2017) suggest that damping and excitation are in near-equilibrium; if that is the case, eccentricity profiles can, in principle, be sustained through the lifetime of the disk.

In the past, the true longevity of eccentricity in simulations has been difficult to ascertain. CBD simulations are subject to slowly-evolving transients that die out on the local viscous timescale. After that, and provided a constant mass supply is available, a steady state can be achieved (Miranda et al. 2017; Muñoz et al. 2019; Moody et al. 2019), in which the CBD reaches a (quasi) stationary density profile (see also Dempsey et al. 2020a). The transient phase exhibits a behavior that is not representative of that of the vastly longer disk lifetime, and it has been argued that many of the accepted outcomes of circumbinary accretion, such as binary migration being inward, have been inferred from simulations in the transient state (Muñoz et al. 2020). Getting past this transient phase is crucial for unveiling the true, long-term eccentricity profile of CBDs, since eccentric modes are sensitive to the background density profile (Teyssandier & Ogilvie 2016; Lee et al. 2019b).

Eccentricity longevity can be verified by comparing simulations to theoretical expectations. If disk eccentricities truly correspond to long-lived modes, and endure over a large number of disk dynamical times, they will have a lasting impact on the binary-disk coupling, as the distributions of torques is bound to be different from that of circular disks, which is the standard assumption of the theory (Goldreich & Tremaine 1980; Artymowicz & Lubow 1994). Additional implications of long-lived eccentricities include the modification the processes taking place within the disk, such as planet formation (e.g. Silsbee & Rafikov 2015), and the use of kinematic observational signatures (e.g., Regály et al. 2011) as an independent diagnosis tool for disk structure.

In this work, we demonstrate that the CBD eccentricities seen in hydrodynamical simulations are consistent with long-lived normal modes. Through a comparison of linear analysis to hydrodynamical simulations in steady-state, we confirm the agreement of the eigenfrequencies and eigenfunctions, finding that the circumbinary cavity size is crucial in determining the spatial extent and the precession rate of eccentricity profiles.

2. LINEAR THEORY OF CIRCUMBINARY ECCENTRICITIES

In simulations of CBDs, an initially circular disk becomes eccentric. Within a rather short time ($\lesssim 1$ viscous time at the CBD inner edge), the eccentricity profile saturates, and thereafter precesses uniformly (Miranda et al. 2017; Thun et al. 2017). The questions of how the eccentricity is excited and then saturates are difficult ones (e.g. Teyssandier & Ogilvie 2016). We hypothesize that the disk's behavior in its saturated state is a normal mode of the disk, and does not depend

on how the eccentricity is excited or saturated. Such a hypothesis is reasonable, provided the mode's precession rate is fast compared to excitation/saturation. In what follows, we calculate the disk's eccentricity profile and precession rate in steady state. However, we do not address the *amplitude* of the mode, which requires one to consider excitation/saturation.

2.1. *Basics of Linear Theory*

The evolution of the complex eccentricity $E = e e^{i\varpi}$, in a locally isothermal 2D disk of density profile Σ and sound speed profile c_s, is governed by

$$2\Sigma R^2\Omega\frac{\partial E}{\partial t} = \frac{i}{R}\frac{\partial}{\partial R}\left(\Sigma c_s^2 R^3\frac{\partial E}{\partial R}\right) + iR\frac{d}{dR}\left(\Sigma c_s^2\right)E - \frac{i}{R}\frac{\partial}{\partial R}\left(\Sigma\frac{dc_s^2}{dR}R^3 E\right) + 2\Sigma R^2\Omega\frac{\partial E}{\partial t}\bigg|_{\rm grav}, \quad (1)$$

(Goodchild & Ogilvie 2006; Teyssandier & Ogilvie 2016; Lee et al. 2019a), with $\Omega(R)$ being the local orbital frequency, and where we have deliberately omitted terms due to excitation and damping (see Introduction). The first three terms on the right-hand side of Equation (1) are due to pressure (the third one being a consequence of a radially varying sound speed; Teyssandier & Ogilvie 2016). The last term is due to a non-Keplerian external potential (Goodchild & Ogilvie 2006). This term can be derived from the disturbing function (e.g., Mardling 2013), after ignoring high-frequency terms (i.e., under the secular approximation). For a circular binary of semi-major axis a_b and mass ratio $q_b = m_2/m_1$, we have, to linear order in E and second order in a_b/R,

$$\frac{\partial E}{\partial t}\bigg|_{\rm grav} = i\Omega f_0(R)E\ , \quad (2)$$

where

$$f_0 = \frac{3}{4}\frac{q_b}{(1+q_b)^2}\left(\frac{a_b}{R}\right)^2\ . \quad (3)$$

If the binary has a finite eccentricity e_b, then the right hand side of Equation (2) includes an additional forcing term $i\Omega f_1(R)E_b$, where $E_b = e_b e^{i\varpi_b}$ is the binary's complex eccentricity, and f_1 is of third order in a_b/R. But throughout this paper, we consider only the case of circular binaries.

2.1.1. *Disks with Central Cavities*

We adopt a surface density profile representative of a CBD in viscous steady state (VSS) (Muñoz & Lai 2016; Miranda et al. 2017; Muñoz et al. 2019)

$$\Sigma(R) = \left[\Sigma_0\left(\frac{R}{a_b}\right)^{-\frac{1}{2}}\right]\left[1-\frac{l_0}{\Omega_b a_b^2}\sqrt{\frac{a_b}{R}}\right]e^{-\left(\frac{R_{\rm cav}}{R}\right)^{\zeta}}\ . \quad (4)$$

The first term in square brackets in Equation (4) is the steady-state solution of a zero-net torque disk with viscosity law $\nu \propto R^{1/2}$ (Lynden-Bell & Pringle 1974), and approximates the CBD solution far from the binary. The second term in square brackets is due to an inner "boundary effect" (Frank et al. 2002; Popham & Narayan 1991), which modifies the perfect power-law profile whenever the advection of angular momentum by the gas crossing the disk's inner edge is not exactly balanced by outward viscous transport (see eq. 19 in Dempsey et al. 2020a). The quantity l_0, introduced by Miranda et al. (2017), is the net torque per unit accreted mass exerted by the CBD on the binary (see also Rafikov 2016),

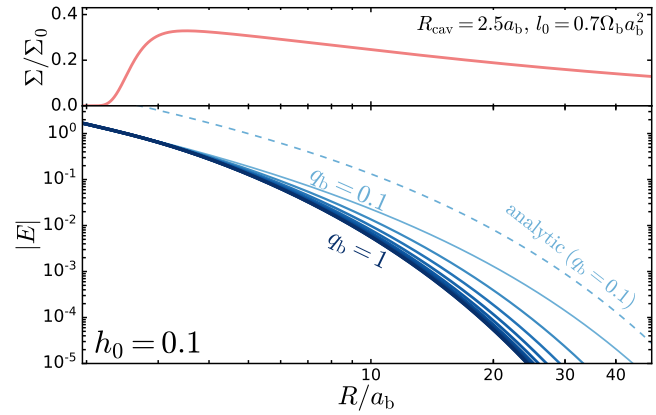

Figure 1. Top: surface density profile (Equation 4) for the fiducial parameters used in this work. Bottom: numerically computed eccentricity eigenfunctions $|E|$ for different values q_b (increasing from lighter to darker blue). The dashed curve corresponds to the analytic estimate of $|E|$ (Equation 12) evaluated at $q_b = 0.1$.

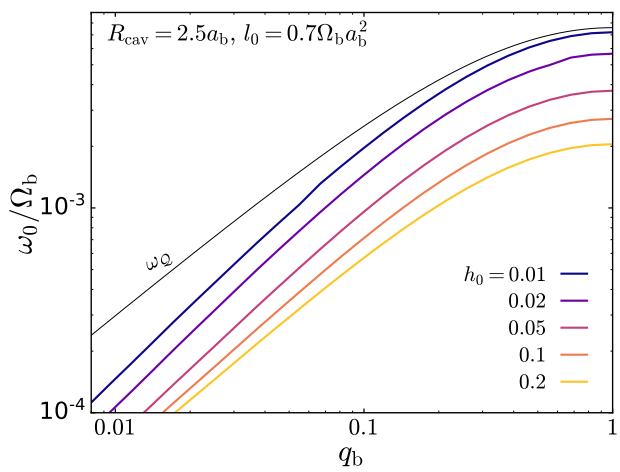

Figure 2. Numerically computed eigenfrequency ω_0 (fundamental mode) in units of Ω_b, as a function of q_b for different values of h_0. For comparison, the test-particle precession rate $\omega_{\mathcal{Q}}$ (Equation 5) is shown as thin black line.

and Ω_b is the binary's orbital frequency. The final exponential factor is the inner cutoff, with two adjustable parameters ζ and $R_{\rm cav}$. In addition, we assume $\Omega = \Omega_b(R/a_b)^{-3/2}$, and that the disk's aspect ratio (h_0) is constant, i.e., $c_s^2 = h_0^2\Omega_b^2 a_b^2(R/a_b)^{-1}$. The main adjustable parameters of the problem are q_b, h_0 and $R_{\rm cav}$. The remaining parameters are fix to $\zeta = 12$ (see Section 3.1 below), and in the present section, to $l_0 = 0.7\Omega_b a_b^2$, which is typical of simulations (Muñoz et al. 2020). A disk profile with fiducial parameters is depicted in the top panel of Figure 1.

2.2. *Numerical Solution of the Boundary Value Problem*

Inserting solutions of the form $E(t,R) = E(R)e^{i\omega t}$ into Equation (1) allows us to replace $\partial E/\partial t$ with $i\omega E$. Together with an appropriate boundary condition the eccentricity equation defines a boundary-value problem (BVP) with eigenvalue ω. This BVP can be solved numerically (e.g. Lee et al. 2019a), and diverse numerical techniques exist for this purpose (e.g. Pryce 1993); in this work, we use a shooting method over a domain $R \in [R_{\rm in}, R_{\rm out}]$. At the boundaries, we impose the boundary condition $\frac{d}{dR}(E/c_s^2) = 0$[1], which is appropriate for

[1] We require that the Lagrangian pressure perturbation $\Delta P = \delta P + RE\frac{dP}{dR}$ vanishes at the disk edges, where δP is the Eulerian perturbation (Lynden-

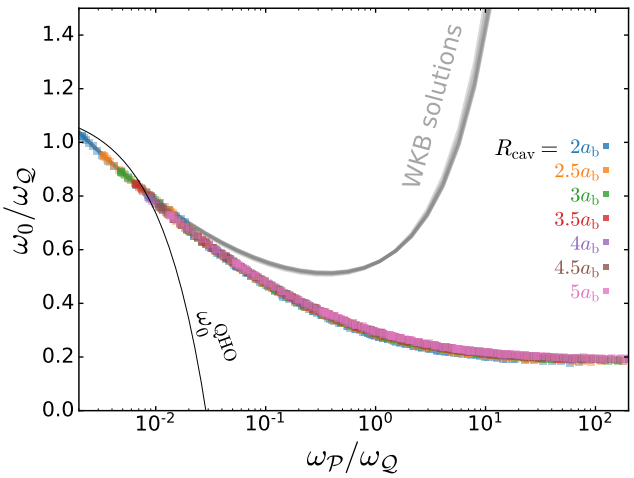

Figure 3. Normalized eigenfrequencies $\omega_0/\omega_{\mathcal{Q}}$ (color squares) as a function of $\omega_{\mathcal{P}}/\omega_{\mathcal{Q}}$ (Equation 5), for a wide range of values in the parameters h_0, $q_{\rm b}$ and $R_{\rm cav}$ (l_0 fixed). Colors denote the values of $R_{\rm cav}$. The approximate analytic frequency $\omega_0^{\rm QHO}$ (Equation 10, thin black line) and the WKB solutions that satisfy the quantization condition (Equation 11, thick gray line) are shown for comparison.

isothermal disks, instead of the condition $dE/dR = 0$, which is adequate for adiabatic perturbations. In general, the choice of boundary condition has an impact on the BVP eigenfunctions and eigenvalues, unless the modes are internally trapped in a resonant cavity away from the boundaries (see Section 2.3 below). For our particular disk model, the type of boundary condition is irrelevant. The computational domain extends from $R_{\rm in} = 0.75R_{\rm cav}$ to $R_{\rm out} = 450a_{\rm b}$. The location of the inner boundary is chosen to optimize convergence speed, but only after the results are checked to be independent of this choice. Robustness against the location of the computational boundary is possible only if the mode is *trapped* (see below), which is a distinct feature of our calculations. By contrast, if a density profile does not naturally trap modes (e.g., a power-law disk) then the eccentricity eigenfunctions and eigenfrequencies will depend sensitively on the location of the computational boundary (Miranda & Rafikov 2018).

In Figure 1 (bottom panel), we show the fundamental mode eccentricity eigenfunctions E for the values of $0.1 \leq q_{\rm b} \leq 1$ typically explored in CBD simulations. These E profiles peak within the cavity, and extend out to several times the binary separation $a_{\rm b}$. However, at distances $R \gtrsim 15a_{\rm b}$, the eccentricity has decreased by 4 orders of magnitude, at which point the disk can be considered to be effectively circular.

In Figure 2, we show the eigenfrequencies ω_0 of the fundamental mode as a function of $q_{\rm b}$ for different values of h_0. These appear to roughly track the quadrupole precession frequency (e.g., Moriwaki & Nakagawa 2004) evaluated at $R_{\rm cav}$:

$$\omega_{\mathcal{Q}} \equiv \frac{3}{4}\frac{q_{\rm b}}{(1+q_{\rm b})^2}\left(\frac{R_{\rm cav}}{a_{\rm b}}\right)^{-2}\Omega_{\rm cav} \tag{5}$$

where $\Omega_{\rm cav} = \Omega|_{R=R_{\rm cav}}$ (MacFadyen & Milosavljević 2008). More precisely, ω_0 is suppressed relative to $\omega_{\mathcal{Q}}$ by a modest reduction factor that weakly depends on h_0. Surprisingly, ω_0 continues to track $\omega_{\mathcal{Q}}$ at very low q_b, where one might have naïvely expected pressure effects to dominate. We explore that behavior in more detail below.

Although there are three adjustable parameters (q_b, h_0, and $R_{\rm cav}$), the nature of the solutions is determined by a single combination of them. Specifically, if we define the pressure-induced precession frequency evaluated at $R_{\rm cav}$ via

$$\omega_{\mathcal{P}} \equiv h_0^2\Omega_{\rm cav} \tag{6}$$

(Goldreich & Sari 2003; Lee et al. 2019a), then the determining parameter is $\omega_{\mathcal{P}}/\omega_{\mathcal{Q}}$, the ratio of the pressure-induced precession rate to the quadrupole rate, evaluated at $R_{\rm cav}$. To show that, we solve the BVP for 1083 different sets of parameters, with $q_{\rm b} \in [0.003, 1]$, $h_0 \in \{0.01, 0.02, 0.05, 0.1, 0.2\}$ and $R_{\rm cav} \in \{2.0, 2.5, 3.0, 3.5, 4.0, 4.5, 5.0\}$ ($l_0 = 0.7\Omega_{\rm b}a_{\rm b}^2$ is held fixed). The resulting eigenfrequencies are depicted in Figure 3, where we show the normalized eigenfrequency $\omega_0/\omega_{\mathcal{Q}}$ versus the ratio of characteristic frequencies $\omega_{\mathcal{P}}/\omega_{\mathcal{Q}}$ (color squares). As can be seen from the figure, the solutions nearly collapse into a single line[2]. The ratio $\omega_{\mathcal{P}}/\omega_{\mathcal{Q}}$ also dictates the shape of the E-eigenfunctions. The eccentricity profiles associated to subset of the 1083 BVPs of Figure 3 is shown in Figure 4 (left panels). When plotted as a function of $R/R_{\rm cav}$, E-eigenfunctions with a given value of $\omega_{\mathcal{P}}/\omega_{\mathcal{Q}}$ line up with each other. When $\omega_{\mathcal{P}}/\omega_{\mathcal{Q}} \ll 1$ (top), the eccentricity profile is confined to the immediate vicinity of the circumbinary cavity; when $\omega_{\mathcal{P}}/\omega_{\mathcal{Q}} \gg 1$ (bottom) the eccentricity profile extends out to $R \gg R_{\rm cav}$.

2.3. *WKB Theory*

2.3.1. *Effective Potential*

WKB theory provides further physical insight into the numerical results presented above. We introduce a rescaled eccentricity, y, defined via $E = y(\Sigma R^3)^{-1/2}$, which removes the first-order derivatives in the BVP (e.g. Lanczos 2012; Gough 2007), and results in

$$\frac{d^2y}{dR^2} + k^2 y = 0\,, \quad \text{with } k^2(\omega, R) = \frac{2\Omega}{c_s^2}\left[\omega_{\rm pot}(R) - \omega\right] \tag{7}$$

where $\omega_{\rm pot}(R)$ is an "effective potential" in units of frequency (e.g., Lee et al. 2019b). Except for the additional factor $2\Omega/c_s^2$, Equation (7) is the time-independent Schrödinger equation in 1D (Ogilvie 2008). For an axisymmetric density profile $\Sigma(R)$, the effective potential is

$$\begin{aligned}\omega_{\rm pot}(R) &= \Omega f_0 + \frac{h_0^2\Omega_{\rm b}}{2}\left(\frac{R}{a_{\rm b}}\right)^{-\frac{3}{2}}\left[\frac{R\Sigma'}{2\Sigma} + \left(\frac{R\Sigma'}{2\Sigma}\right)^2 - \frac{R^2\Sigma''}{2\Sigma} - \frac{3}{4}\right] \\ &= \omega_{\mathcal{Q}}\left(\frac{R}{R_{\rm cav}}\right)^{-\frac{7}{2}} \\ &\quad + \frac{\omega_{\mathcal{P}}}{2}\left(\frac{R}{R_{\rm cav}}\right)^{-\frac{3}{2}}\left[\frac{R\Sigma'}{2\Sigma} + \left(\frac{R\Sigma'}{2\Sigma}\right)^2 - \frac{R^2\Sigma''}{2\Sigma} - \frac{3}{4}\right]\end{aligned} \tag{8}$$

where primes denote radial derivatives. The first term on the right hand side of Equation (8) is the "quadrupole contribution" (e.g., Moriwaki & Nakagawa 2004). The remaining terms are the "pressure contribution," which depend on the Σ profile, but not its normalization.

Bell & Ostriker 1967) and RE is the radial Lagrangian displacement (Papaloizou 2002). From the continuity equation, and assuming a locally isothermal equation of state, $\delta P = -c_s^2 R\frac{d}{dR}(E\Sigma)$, and thus $\Delta P = -R\Sigma c_s^4\frac{d}{dR}(E/c_s^2)$.

[2] An exact collapse of the curves into a perfect line can be achieved by setting $l_0 = 0$ or by rescaling l_0 such that $l_0 R_{\rm cav}^{-1/2}$ =constant.

The sign of $\omega_{\rm pot}$ helps us determine the sign of ω, i.e., whether modes are prograde or retrograde (e.g. Teyssandier & Ogilvie 2016). For instance, the quadrupole contribution is the precession rate of a test particle around a binary and is always positive. On the other hand, the pressure contribution is small and negative far from the cavity, as in for pure power-law disks (e.g., Goldreich & Sari 2003; Miranda & Rafikov 2018), but it becomes positive near the cavity edge. As we show below, all of our modes are prograde, even when pressure dominates over the quadrupole.

When the circumbinary cavity is included, $\omega_{\rm pot}$ develops a local maximum, which is crucial for the existence of trapped modes. The function $\omega_{\rm pot}$ (depicted in Figure 5, left panel) exhibits a general shape that consists of a repulsive ($\omega_{\rm pot} \to -\infty$) inner region and attractive ($\omega_{\rm pot} > 0$) "potential well" [3], that peaks at $R_{\rm peak} = gR_{\rm cav}$ with g of order unity. The potential well can result in trapped modes ("bound states") within that region provided that the peak is tall enough[4]. The potential well is accompanied two turning points, beyond which waves cannot propagate. In the "classically forbidden region" depicted in gray in Figure 5, the y-eigenfunctions are evanescent. Oscillatory solutions are allowed outside the "potential well", but only in the form of traveling waves ("free states") of negative frequency.

The trapping of the y-eigenfunctions can be seen in the right panels of Figure 4. These profiles are strongly-peaked functions with exponential cutoffs due to the left and right turning points (when $\omega = \omega_{\rm pot}$). The left exponential cutoff is largely independent of $\omega_{\mathcal{P}}/\omega_{\mathcal{Q}}$; conversely, the right cutoff depends sensitively on $\omega_{\mathcal{P}}/\omega_{\mathcal{Q}}$, with larger values producing more delocalized eigenfunctions.

2.3.2. *Approximate Eigenfrequencies*

The sharp local maximum in $\omega_{\rm pot}$ suggests that we can study eigenmodes trapped deeply into the potential well by expanding to low order in R and looking for known solutions of the time-independent Schrödinger equation. First, we write Equation (7) in "Liouville normal form" (Liouville 1837; Amrein et al. 2005) to eliminate the pre-factor multiplying ω. With a change of variables $y = Y(R/R_{\rm cav})^{1/8}$, $\xi = (R/R_{\rm cav})^{3/4}$, we have

$$\frac{9\omega_{\mathcal{P}}}{32}\frac{d^2Y}{d\xi^2} + \left[\omega_{\rm pot}[R(\xi)] - \frac{7\omega_{\mathcal{P}}}{128}\xi^{-2}\right] Y = \omega Y \tag{9}$$

Second, we expand the pressure-dependent term in $\omega_{\rm pot}$ around the local maximum $\xi_{\rm peak}$ to second order in ξ and evaluate the remaining terms at $\xi = \xi_{\rm peak}$, i.e., the term in square bracket in Equation (9 is approximated by a quadratic potential. Therefore, the resulting expression can be cast into the standard Schrödinger equation for the quantum harmonic oscillator (QHO), and thus the eigenfrequencies in Equation (9) are given by:

$$\omega_n^{\rm QHO} \approx 1.13\omega_{\mathcal{Q}} + 26.1\omega_{\mathcal{P}} - 130\omega_{\mathcal{P}}\left(n+\frac{1}{2}\right) \tag{10}$$

(see Appendix B). Equation (10) is depicted in Figure 3 (thin black line) for $n = 0$. When $\omega_{\mathcal{P}}/\omega_{\mathcal{Q}} \ll 1$, the analytic $\omega_0^{\rm QHO}$ and the BVP frequencies show a moderate level of agreement, indicating that the modes are rarely deep enough into the potential well to be properly described with this local expansion.

2.3.3. *WKB Eigenfrequencies from the Quantization Condition*

The WKB method of elementary quantum mechanics can be directly applied to obtain the solutions to Equation (7), provided k is sufficiently large compared to the lengthscale of variation of $\omega_{\rm pot}$. Trapped modes are those with discrete eigenvalues ω_n that satisfy the Einstein-Brillouin-Keller quantization condition (Einstein 1917; Keller 1958), which is given by

$$\oint k(\omega_n, R)dR = \left(2n + \frac{\mu}{2}\right)\pi \tag{11}$$

where k is from the dispersion relation (Eq. 7), and μ is the amount of phase loss, sometimes called the Maslov index[5]. In this case, $\mu = 2$, which is the number of classical turning points for a 1D potential like $\omega_{\rm pot}$ (Mark 1977; Shu et al. 1990; Lee et al. 2019a).

The behavior of a trapped mode is further illustrated in the dispersion relation map (DRM) of Figure 5 (right panel), which depicts constant-ω contours of the dispersion relation (Equation 7) for different values of R and kR. Traveling waves propagate along open contours, while trapped modes (standing waves) trace closed loops. For the example of the figure, the quantization condition is satisfied by one and only one such closed loop (for $n = 0$, in red). The existence of just one trapped mode is a general property of CBDs with $h_0 \sim 0.1$, which is the typical aspect ratio of of most CBD simulations (e.g., Farris et al. 2014; Miranda et al. 2017; Muñoz et al. 2019; Duffell et al. 2019). Colder disks ($h_0 \lesssim 0.05$), on the other hand, can support higher-n modes (Appendix A). This type of disk has been simulated recently (Thun et al. 2017; Tiede et al. 2020), but no multi-harmonic disk eccentricity has been reported.

Figure 3 also includes the WKB frequencies as a function of $\omega_{\mathcal{P}}/\omega_{\mathcal{Q}}$. The agreement with the BVP frequencies is excellent for $\omega_{\mathcal{P}}/\omega_{\mathcal{Q}} < 1$, but the two solution quickly diverge when $\omega_{\mathcal{P}}/\omega_{\mathcal{Q}} > 1$, i.e., at low eigenfrequencies. To understand this discrepancy, we turn to studying the WKB eigenfunctions below.

2.3.4. *Approximate Eccentricity Profiles*

Far from the cavity, we can write the evanescent part of the y-eigenfunction using the WKB approximation $y \sim \exp[-\int dR(-k^2)^{1/2}]$. For $\omega \gg |\omega_{\rm pot}|$, we obtain

$$E \sim R^{-5/4}\exp\left[-\left(\frac{R}{\lambda}\right)^{3/4}\right] \tag{12}$$

where

$$\lambda = R_{\rm cav}\left(\frac{9}{32}\frac{\omega_{\mathcal{P}}}{\omega_0}\right)^{2/3} \tag{13}$$

i.e., the eccentricity profile is a tapered power-law with tapering radius λ (see also appendix C in Shi et al. 2012). A rough approximation of the quantization condition gives $\lambda \sim R_{\rm cav}(\omega_{\mathcal{P}}/\omega_{\mathcal{Q}})^{2/3}[1 - 0.02(\omega_{\mathcal{Q}}/\omega_{\mathcal{P}})]$ (Appendix C). Equation (12) is included in Figure 1 (for clarity, only for the $q_{\rm b} = 0.1$ case). The tapering effect is a natural consequence of

[3] Note that it is the negative of $\omega_{\rm pot}$ that corresponds to the quantum mechanical potential.

[4] Asymmetric potential wells in 1D do not guarantee the existence of bound states (Landau & Lifshitz 1981, §22), while symmetric wells always have a ground state (Simon 1976).

[5] The Maslov index corresponds to the number of turning points through a smooth potential (i.e., a soft reflection) plus *twice* the number of turning points under Dirichlet boundary conditions (i.e. a hard reflection).

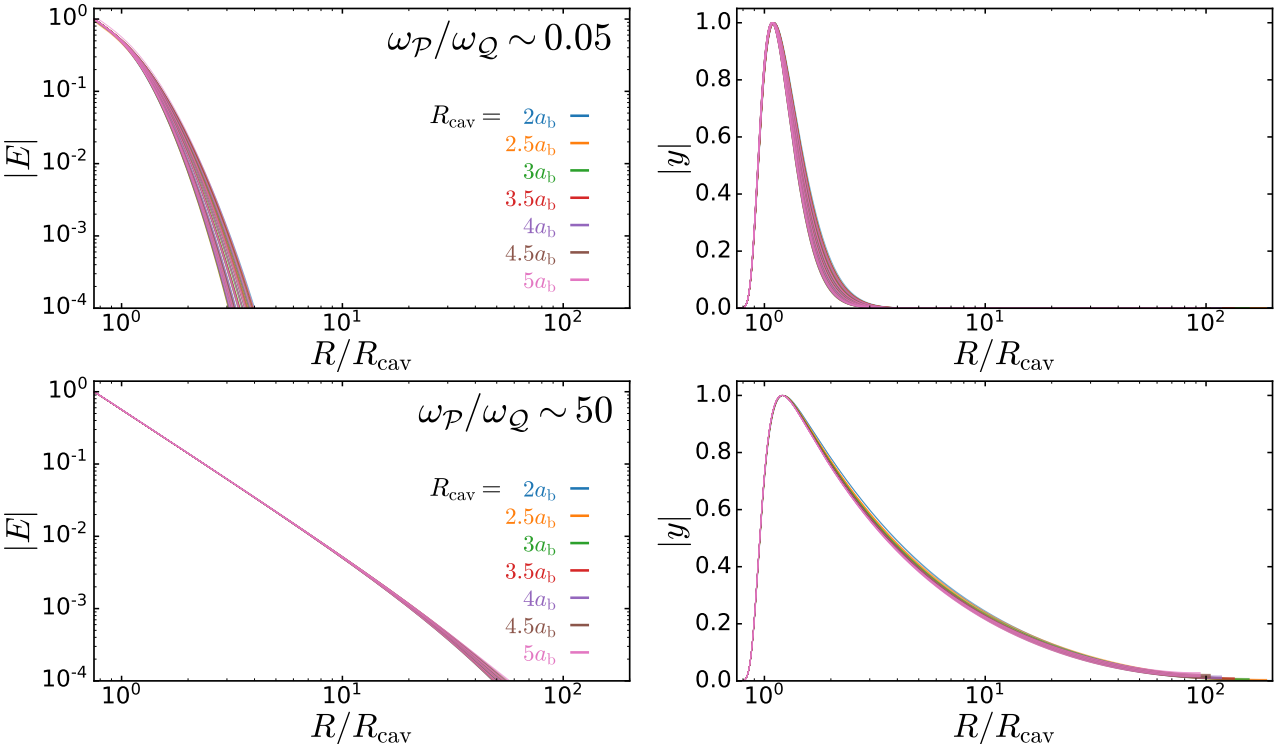

Figure 4. Left panels: multiple eccentricity eigenfunctions E obtained from the numerical solution to the BVP for $0.0375 < \omega_{\mathcal{P}}/\omega_{\mathcal{Q}} < 0.075$ (top) and $37.5 < \omega_{\mathcal{P}}/\omega_{\mathcal{Q}} < 75$ (bottom). Right panels: rescaled eccentricity $|y| = |E|(\Sigma R^3)^{1/2}$ corresponding to the E-eigenfunctions in the right panels. Color denotes the value of $R_{\rm cav}$ as in Figure 3.

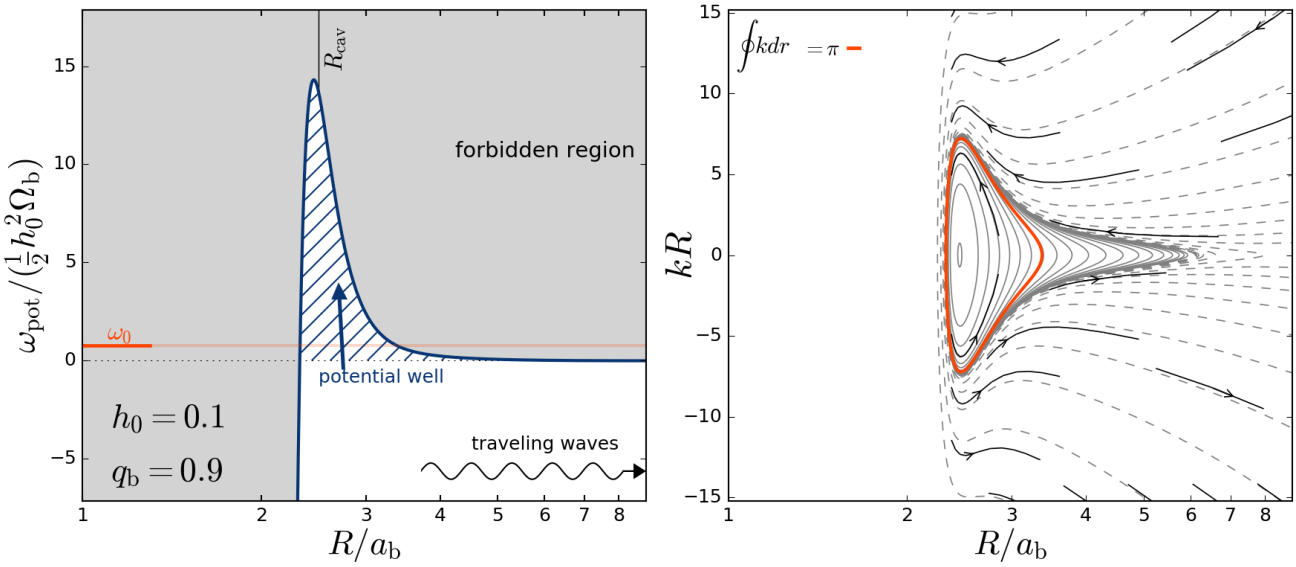

Figure 5. Left panel: effective potential $\omega_{\rm pot}$ (blue curve, Equation 8) for fiducial parameters and $h_0 = 0.1$ and $q_{\rm b} = 0.9$ ($\omega_{\mathcal{P}}/\omega_{\mathcal{Q}} = 0.33$). Forbidden, trapped, and traveling-wave regions are labeled (see text). The red line depicts the fundamental frequency ω_0 that satisfies the quantization condition (11) with $n = 0$. Right panel: WKB dispersion relation map (DRM) (Tremaine 2001; Lee et al. 2019a) depicting the the contours of constant frequency ω in $R-kR$ space. Negative frequencies (dashed contours) allow for outgoing ($kR < 0$) and incoming waves ($kR > 0$). Positive frequencies (solid contours) exhibit two turning points, resulting in closed loops. The highlighted contour in red satisfies $\oint kdR = \pi$.

the y-eigenfunction being a trapped mode. Note that, in Equation (13), λ is arbitrarily large for arbitrarily small ω, which is the usual behavior of marginally bound states in quantum mechanical potential wells. This "delocalization" of the eigenfunctions explains the radial extent of E and y in Figure 4, in turn explaining why WKB fails at low frequencies, since the spatial wave number is too small for the approximation to hold. As a consequence, when $\omega_{\mathcal{P}}/\omega_{\mathcal{Q}} \to \infty$ (i.e., when the quadrupole contribution is negligible), eigenfunctions are not trapped, even if the CBD is steeply truncated around the binary.

We may now also qualitatively understand the surprising result that $\omega_0 \sim \omega_{\mathcal{Q}}$ (Figures 2 and 3), even when when pressure naively dominates over the quadrupole ($\omega_{\mathcal{P}}/\omega_{\mathcal{Q}} \gg 1$). The reason behind this result is that, when $\omega_{\mathcal{P}}/\omega_{\mathcal{Q}}$ is large, the delocalized eigenfunction extends out to many times $R_{\rm cav}$, in which case the pressure-induced precession rate is much lower than the naive expectation $\omega_{\mathcal{P}} \sim h_0^2\Omega_{\rm cav}$. Instead, the magnitude of the pressure-induced precession is set by the value of $h_0^2\Omega$ at $R \gg R_{\rm cav}$, where the eigenfunction is within a factor of a few of its peak value. At these distances, $h_0^2\Omega$ is much less than $\omega_{\mathcal{P}}$, and can never overcome quadrupole-induced precession.

3. COMPARISON TO HYDRODYNAMICAL SIMULATIONS

3.1. *Hydrodynamics of Circumbinary Accretion*

We carry out 2D hydrodynamics simulations of steady-state CBDs using the moving-mesh code AREPO (Springel 2010; Pakmor et al. 2016) in its Navier-Stokes formulation (Muñoz et al. 2013), using a locally isothermal equation of state ($c_s^2 \propto R^{-1}$) and an α-viscosity prescription. Once transients die out, these simulations are fully determined by four parameters: $q_{\rm b}$, $e_{\rm b}$, h_0 and the viscosity coefficient α. We focus on the case $e_{\rm b} = 0$ and vary the other parameters, restricting ourselves to the regime with $h_0 \sim 0.1$, which, from WKB analysis, is expected to develop a single trapped mode. We note that α does not appear in the linear calculations (Section 2).

Details on the model setup and numerical scheme can be found in Muñoz & Lai (2016), Muñoz et al. (2019) and Muñoz et al. (2020). The general findings of the aforementioned works include:

- A boundary condition with constant mass supply $\dot{M}_0$ enables CBDs to reach viscous steady state (VSS) (see also Miranda et al. 2017; Dempsey et al. 2020a). Once VSS is reached, the binary accretion rate $\dot{M}_{\rm b}$ equals (on average) the supply rate $\dot{M}_0$.

- In VSS, the net angular momentum current in the CBD $\dot{J}_{\rm d}$ (including advective, viscous and gravitational contributions) is statistically stationary and independent of radius (Miranda et al. 2017). In addition, the time average $\langle \dot{J}_{\rm d} \rangle$ equals the net angular momentum transfer rate from the disk onto the binary $\langle \dot{J}_{\rm b} \rangle$ (which is comprised of gravitational and accretional torques).

- Most importantly, the quantity $l_0 \equiv \langle \dot{J}_{\rm b} \rangle / \langle \dot{M}_{\rm b} \rangle$ is a positive constant. If $l_0 > l_{0,\rm crit}$ (where $l_{0,\rm crit} > 0$ depends on the binary properties; Muñoz et al. 2020), then the accretion process leads to binary expansion.

CBD simulations in VSS and positive l_0 produce stationary Σ profiles that exhibit mass *deficits* in relation to the power-law profiles of equal accretion rate[6]. Planetary-mass companions, by contrast, have $l_0 < 0$ and exhibit mass pile-ups (e.g., Dempsey et al. 2020a). These stationary Σ profiles are well described by Equation (4), which is a function of three parameters: Σ_0, l_0 and $R_{\rm cav}$ ($\zeta = 12$ is held fixed). Moreover, in VSS, $\Sigma_0 = \dot{M}_0/(3\pi\alpha h_0^2\Omega_{\rm b}a_{\rm b}^2)$, and l_0 can be computed from the torque balance in the simulations; hence, the only remaining parameter for the Σ profile is the cavity size $R_{\rm cav}$, which we fit from time-averaged density profiles.

In Figure 6, we show examples of the measured Σ (in blue) contrasted to the parametric model (Equation 4, in red) with best-fit values of $R_{\rm cav}$ for two different simulations with $h_0 = 0.1$ ($q_{\rm b} = 0.2$, $\alpha = 0.1$ on top, and $q_{\rm b} = 0.8$, $\alpha = 0.05$ at the bottom). With a fully determined Σ profile and sound-speed profile, we can compute the linear eigenfunctions and eigenfrequencies for a suite of hydrodynamical models (see Section 3.3 below).

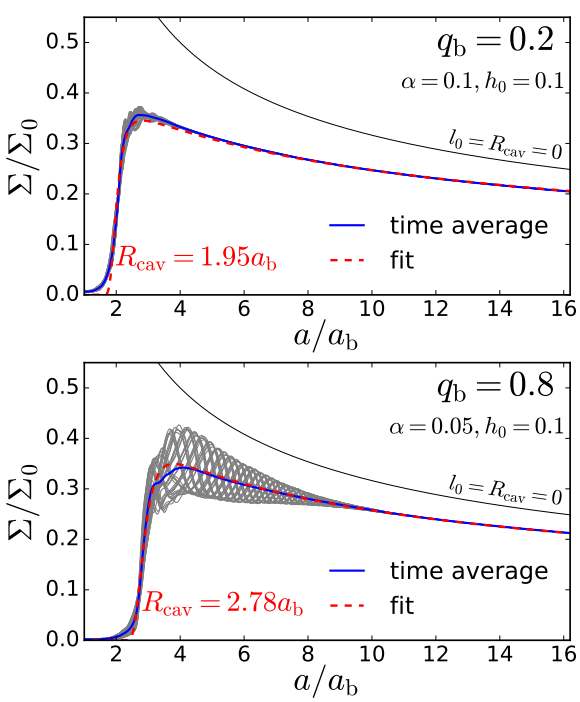

Figure 6. Examples of the time-averaged surface density profiles of CBDs in VSS, where the radial coordinate is the semimajor axis ratio $a/a_{\rm b}$. Top panel: Σ profile of a disk with $\alpha = h_0 = 0.1$ around a circular binary of mass ratio $q_{\rm b} = 0.2$. Gray curves depict individual snapshots of the density field; their time average (over 500 binary orbits) is depicted by the blue curve; the dashed red line is the best-fit model (Equation 4). Bottom panel: same as above but for $q_{\rm b} = 0.8$. In both panels, the thin black line depicts the power-law profile $\Sigma = \Sigma_0(a/a_{\rm b})^{-1/2}$, i.e., the torque-free solution with $l_0 = R_{\rm cav} = 0$ at the same accretion rate $\dot{M}_0$. As is well-known, positive values of l_0 are tantamount to a density deficit relative to the power-law solution.

3.2. *Freely Precessing Eccentric Disks*

CBD simulations are known to develop lopsided cavities which change orientation on time-scales much longer than the binary's orbital period (e.g., MacFadyen & Milosavljević 2008; Miranda et al. 2017; Thun et al. 2017). This slowly

[6] This deficit is also a well-known consequence of the (misleadingly labeled) "zero-torque boundary condition" at some finite radius (Lynden-Bell & Pringle 1974; Frank et al. 2002; Dempsey et al. 2020b). Recently, however, Tiede et al. (2020) has reported *pileups*, rather than deficits, in simulations of cold ($h_0 \lesssim 0.04$) CBDs, which translate into negative values of l_0.

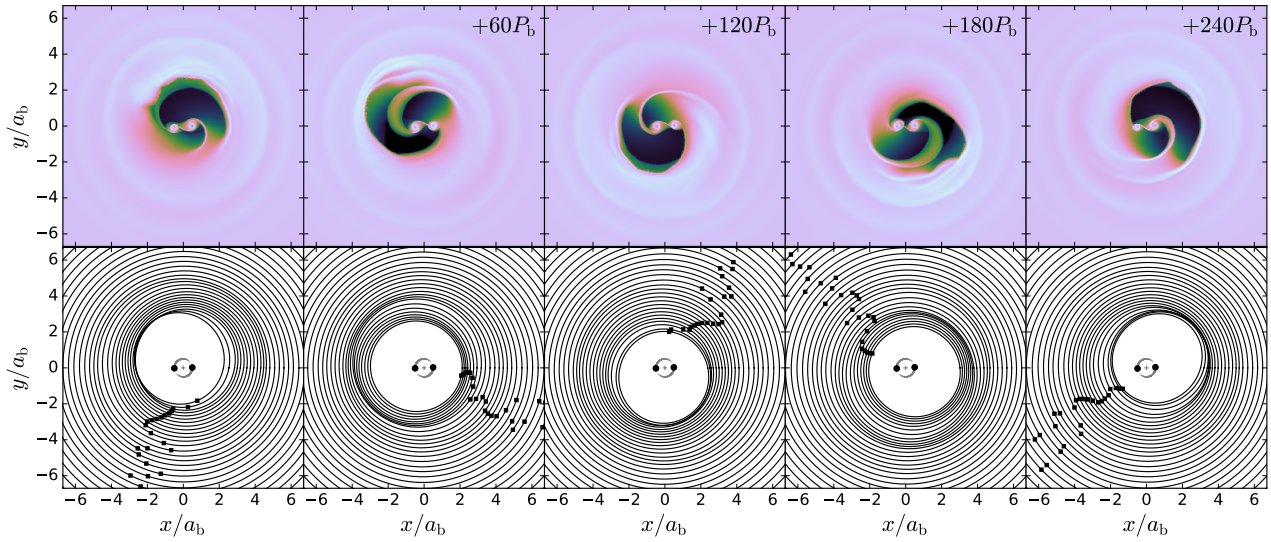

Figure 7. Evolution of CBDs over secular timescales. Top panels: surface density (logarithmic scale) in the vicinity of a binary with $q_b = 1$, $e_b = 0$ (disk parameters are $h_0 = \alpha = 0.1$) in intervals of 60 binary orbits once steady-state has been achieved. The gas morphology is consistent throughout the panels, except for the orientation of the central cavity, which evolves in tandem with the disk eccentricity. Bottom panels: barycentric elliptical "orbits" corresponding to gas eccentricity (Equation 14) binned in semi-major axis, These "orbits" change in time, exhibiting prograde apsidal precession, as evidenced by the advancement of the longitude of pericenter ϖ_d, depicted by solid black squares; the orientation of the ellipses is roughly coherent (ϖ_d is approximately equal for all radii) out to a distance of $\sim 10a_b$ from the barycenter. For this simulation, a fit of the parametric model (4) to the surface density gives $R_{cav} = 2.42a_b$.

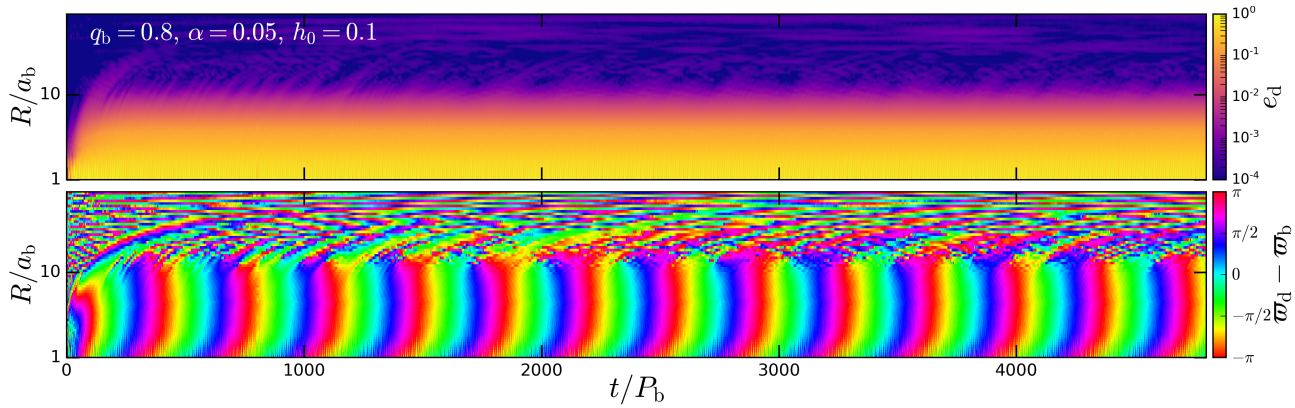

Figure 8. Eccentricity evolution maps for a CBD with $h_0 = 0.1$ and $\alpha = 0.05$ around a circular binary with $q_b = 0.8$. For this simulation, a fit of the parametric model (4) to the surface density gives $R_{cav} = 2.78a_b$.

varying lopsidedness can be readily appreciated in in Figure 7 (top panels), which shows the surface density every 60 binary orbits for total time interval of 240 binary orbits.

One can compute a "dynamic" eccentricity from the velocity field (e.g., MacFadyen & Milosavljević 2008). As in Miranda et al. (2017), we measure disk eccentricity by first computing the Laplace-Runge-Lenz vector of the i-th gas cell (see also Teyssandier & Ogilvie 2017)

$$\mathbf{e}_i = \frac{1}{\Omega_b^2 a_b^3}\mathbf{v}_i \times (\mathbf{r}_i \times \mathbf{v}_i) - \frac{\mathbf{r}_i}{|\mathbf{r}_i|} \quad . \tag{14}$$

which can be combined into a global eccentricity vector $\mathbf{e}_d$. By binning cells in semi-major axis, we can construct a set of co-focal Keplerian orbits, as shown in the bottom panels of Figure 7. These ellipses match the orientation and precession rate of the lopsided cavity. More importantly, the ellipses exhibit apsidal coherence (the longitudes of pericenter are aligned), meaning that they precess in tandem, which is suggestive of proper mode behavior.

The time evolution of the disk eccentricity can be better assessed from space-time eccentricity maps. Following Miranda et al. (2017), we bin the gas eccentricity vector $\mathbf{e}_i$ in barycentric radius to obtain $\mathbf{e}_d$ as a function of R and t. We visualize the eccentricity $e_d = (e_{d,x}^2 + e_{d,y}^2)^{1/2}$ (top) and the longitude of pericenter $\varpi_d = \tan^{-1}(e_{d,x}, e_{d,y})$ (bottom) as intensity maps. The maps of Figure 8 correspond to a simulation with $q_b = 0.8$, $h_0 = 0.1$ and $\alpha = 0.05$ integrated for $\simeq 5000$ binary orbits. Eccentricity growth is rapid: the e_d map saturates after $\simeq 200P_b$ and remains time-independent afterward. The ϖ_d map achieves a regularly repeating pattern after a few hundred binary orbits, showing that the disk precesses continuously, spanning the range $[0,2\pi]$ at a fixed rate.

One can further define a global longitude of pericenter $\overline{\varpi}_d \equiv \tan^{-1}(\overline{e}_{d,x}, \overline{e}_{d,y})$ (Fig. 8, bottom panel) where $\overline{e}_{x,y} \equiv \int \Sigma e_{x,y} R dR / (\int \Sigma R dR)$ denotes a mass-weighted radial average of the eccentricity vector over the entire disk. The global precession frequency,

$$\dot{\varpi}_d \equiv \frac{d}{dt}\overline{\varpi}_d \ , \tag{15}$$

in the example of the figure, is $\dot{\varpi}_d = 2.77 \times 10^{-3}\Omega_b$. Hydrodynamical simulation typically exhibit precession rates

$\sim \mathcal{O}(10^{-3}\Omega_b)$ (MacFadyen & Milosavljević 2008; Miranda et al. 2017), which is consistent with the quadrupole-induced precession rate at the edge of the cavity.

3.3. *Comparison of Theory and Simulations*

As a test of the validity of the linear eccentricity equation (1), we compare the hydrodynamic eccentricity profiles and precession rates to the eigenfunctions and eigenfrequencies, respectively, obtained from solving the BVP. The WKB approximation is not expected to hold, since our simulations have $\omega_{\mathcal{P}}/\omega_{\mathcal{Q}} \simeq 0.3-0.4$, which is slightly outside the regime in which the WKB approximation is valid (see Figure 3).

Figure 9 shows the eccentricity profiles obtained from hydrodynamics (squares) and the linear BVP (lines) for q_b =0.2, 0.4 and 1 and three different combinations of h_0 and α. In each case, the values R_{cav} and l_0 used in the BVP are extracted from simulations. The profiles show good agreement, revealing that the tapered power-law behavior of $|E|$ (Equation 12) is representative of the eccentricity behavior in hydrodynamical simulations. The difference between the panels is subtle, although the dependence on viscosity is clear: in general, a higher α corresponds to a smaller R_{cav} (e.g., Artymowicz & Lubow 1994; Miranda & Lai 2015). Consequently, high viscosity shifts the eccentricity profile inward (see Equation 12).

Similarly, we can compare the empirical precession rate $\dot{\varpi}_d$ (Equation 15) to the linear eigenfrequency ω_0. In general, the linear frequencies are within around 50% of the hydrodynamical ones, and the high viscosity case (middle panel) shows a remarkable agreement between the two approaches.

4. DISCUSSION

An exhaustive understanding of how disk and binary eccentricities couple to each other is still lacking. In this work, we have taken a first step toward a full picture of disk eccentricity by showing that CBDs naturally tend to trap eccentric modes in the vicinity of the central cavity. The turning points that allow for the trapping of waves are a consequence of the steeply but smoothly truncated CBD profile, which makes our results independent of the boundary conditions.

4.1. *Importance of eccentric disks*

The inevitability of freely precessing disks around binaries can introduce an important change into our understanding of the physical processes in circumbinary environments. Long-lived disk eccentricities can (1) determine the dynamical coupling of binaries and disks; (2) modify the physical processes within protoplanetary disks, such as circumbinary planet formation, and (3) potentially leave observable imprints in the gas kinematics and disk morphologies.

A theoretical understanding of CBD eccentricity profiles might aid the interpretation of observational data. Recently, the "binary interpretation" of transitional disks (Ireland & Kraus 2008) has attracted renewed interest as a result of the rich morphological and kinematic signatures observed in astrophysical disks (see., e.g., Price et al. 2018, for the case of HD142527). Self-consistent eccentricity profiles will prove powerful tools as a diagnostic for hidden binaries and disk properties.

Moreover, eccentricity profiles inferred from observations can provide independent information on a disk's density and temperature profiles. For example, Equation (12) is derived assuming that far from the cavity $\Sigma \propto R^{-1/2}$ (in turn a consequence of $\nu \propto R^{1/2}$) and that $c_s^2 \propto R^{-1}$, but a different set of assumptions would result in different eccentricity profiles.

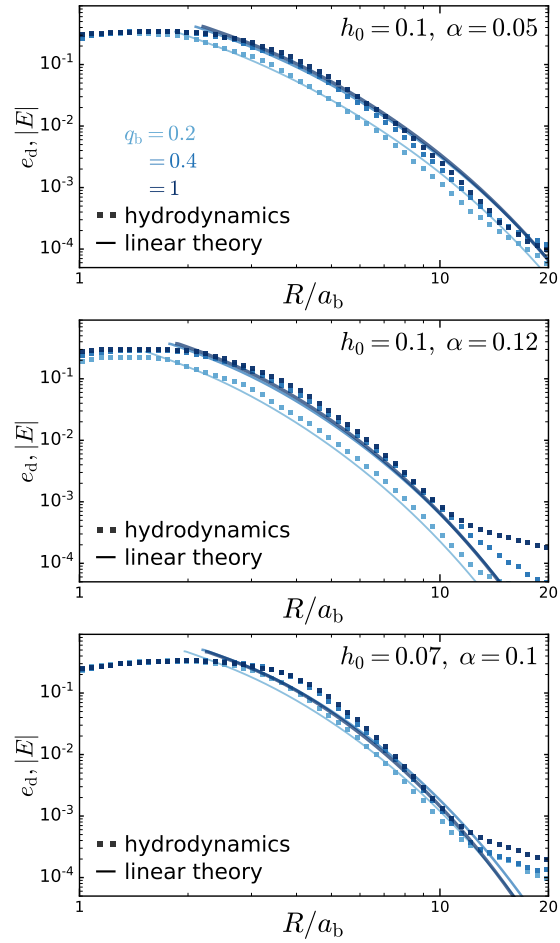

Figure 9. Eccentricity eigenfunctions E derived from linear analysis (solid lines) compared to the empirical eccentricity profiles e_d measured directly from hydrodynamical simulations (small square markers) as described in Section 3.2. Each panel consists of three different binary mass ratios (q_b = 0.2, 0.4 and 1, from dark blue to light blue) and panels differ in their combination of h_0 and α. For each set of mass ratios $q_b = (0.2, 0.4, 1)$ the cavity sizes are $R_{cav} = (2.32a_b,\ 2.64a_b,\ 2.79a_b)$ (top), $R_{cav} = (1.90a_b,\ 2.22a_b,\ 2.33a_b)$ (middle), and $R_{cav} = (2.48a_b,\ 2.78a_b,\ 2.86a_b)$ (bottom). The normalization of the linear eigenfunctions is arbitrary, and is chosen to match the hydrodynamical eccentricity at the edge of the cavity.

4.2. *Three-dimensional Effects*

In this work, we have focused on gas eccentric modes in two dimensions, since most long-term hydrodynamical simulations are 2D. However, in 3D, the RHS Equation (1) includes the additional term $\frac{3}{2}i\Sigma\frac{d}{dR}(c_s^2R^2)E$ (Ogilvie 2008; Teyssandier & Ogilvie 2016), which depends on Σ but not on its derivative, and thus is always positive. However, the 2D pressure terms in the vicinity of R_{cav} –where the trapped mode lives– are already positive, thanks to the steep gradients in Σ. Thus, the 3D term can increase the eigenfrequency, but not change its sign. The role of the additional term is made clear by transforming the 3D eccentricity equation into normal form, repeating the procedure of Section 2.3.1. The effective potential now becomes

$$\omega_{pot}^{(3D)} = \omega_{\mathcal{Q}}\left(\frac{R}{R_{cav}}\right)^{-\frac{7}{2}} + \\ + \frac{\omega_{\mathcal{P}}}{2}\left(\frac{R}{R_{cav}}\right)^{-\frac{3}{2}}\left[\frac{R\Sigma'}{2\Sigma} + \left(\frac{R\Sigma'}{2\Sigma}\right)^2 - \frac{R^2\Sigma''}{2\Sigma} + \frac{3}{4}\right] \tag{16}$$

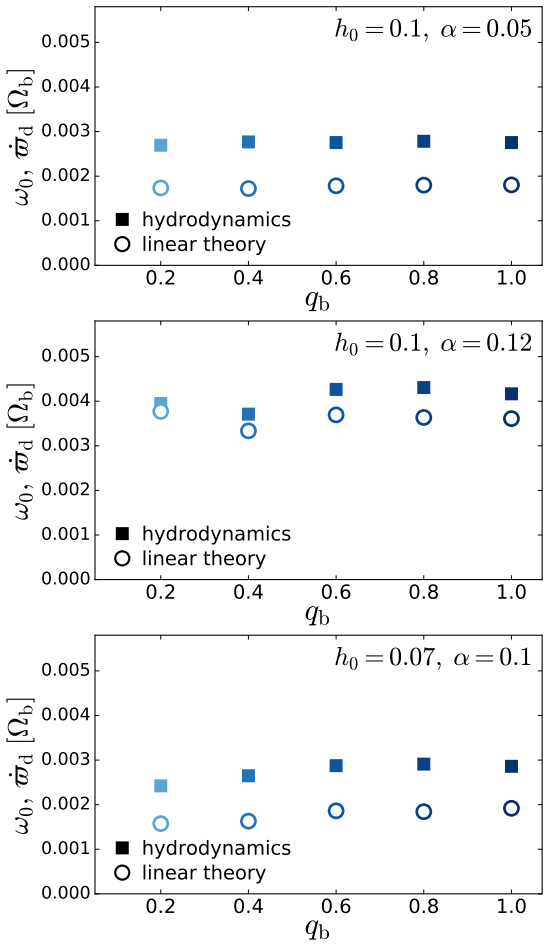

Figure 10. Linear fundamental-mode eigenfrequencies ω_0 (circles) corresponding to the eigenfunctions of Figure 9, compared to empirically measured precession frequencies $\dot{\varpi}_d$ (squares) as given by Equation (15). The order of the panels is the same as in Figure 9.

Remarkably, the only difference between $\omega_{\rm pot}$ (Equation 8) and $\omega_{\rm pot}^{(3D)}$ (Equation 16) is the numerical factor of $\pm\frac{3}{4}$ inside the square brackets, which is much smaller than the Σ-dependent terms near the peak of the effective potential (Figure 5, left panel). Consequently, eccentric modes are essentially unaffected by 3D terms provided that they are confined by turning points. Note that the radial coordinate in $\omega_{\rm pot}^{(3D)}$ scales with $R_{\rm cav}$, which implies that larger cavities would simply displace the mode further out and slow down the precession rate, but not change the sign of ω_0. The robustness of eccentric mode trapping might explain why Moody et al. (2019) found no major differences between 2D and 3D (coplanar) simulations of circumbinary accretion.

4.3. *Future work: eccentric binaries*

In this work, we have limited ourselves to the study of circular binaries. Evidently, a comprehensive study of binary disk interaction must include eccentric binaries, since these binaries are known to exist in the T Tauri phase of stellar evolution (e.g. Tofflemire et al. 2017, 2019). The gas dynamics around moderate-to-high eccentricity binaries is rich and complex, and can differ substantially from their circular counterparts (Muñoz & Lai 2016). Eccentric binaries accreting from VSS disks might see their eccentricity damped or excited (Muñoz et al. 2019), suggesting that there may exist an equilibrium eccentricity at $e_b \sim 0.2-0.4$ (see also Roedig et al. 2011), in analogy to a similar phenomenon observed for migrating gas giants (Duffell & Chiang 2015). Precessing eccentric disks around binaries may be the culprits of the "alternating preferential accretion" phenomenon (Dunhill et al. 2015; Muñoz & Lai 2016), which could explain why primary accretion is dominant in the eccentric T Tauri binary TWA 3A Tofflemire et al. (2019), despite most simulations suggesting that preferential accretion is invariably onto the secondary (e.g., Bate 2000; Farris et al. 2014; Muñoz et al. 2020).

For finite binary eccentricity e_b, the general solution E will thus consist of a complementary (homogeneous) solution and a particular one, i,e., a "free" mode accompanied by a "forced" mode. In principle, for large enough forced eccentricity, the disk's eccentricity vector will rotate around the tip of the forced eccentricity rather the origin, i.e., ϖ_d will librate instead of circulating. In upcoming work, we will simulate CBDs around eccentric binaries, probing the limitations of linear theory.

5. SUMMARY AND CONCLUSIONS

We have studied the properties of eccentricity modes in accretion disks around circular binaries using linear analysis and direct hydrodynamical simulations. Our findings are:

(*i*) A linear eigenmode analysis shows that steeply truncated circumbinary disks trap eccentricity modes between naturally arising turning points. Often, only one fundamental mode of low frequency $\omega_0 \sim \mathcal{O}(10^{-3}\Omega_b)$ is allowed. This mode precesses in a prograde way, and ω closely tracks ω_Q –the test-particle precession rate around a binary– even when pressure appears to dominate over the quadrupole.

(*ii*) The linear analysis shows that, when $q_b \lesssim 1$, the eccentricity profiles are concentrated toward the edge of the circumbinary cavity (at a radius of $2a_b$), and decrease in a tapered power-law fashion, with an exponential drop-off at $\sim 10a_b$. For $q_b \ll 1$ and/or $h_0 \gtrsim 0.2$, the modes are poorly confined, effectively extending out to many times the binary separation a_b.

(*iii*) We have carried out non-linear hydrodynamical simulations of circumbinary disks in viscous steady state for $0.2 \le q_b \le 1$ and different values of h_0 and α. These simulations develop a steady-state, coherently precessing eccentricity profile. The precession rates and the radial dependence of the eccentricity are in good agreement with our analytical and numerical linear calculations, confirming that simulations around circular binaries develop free modes sustained by the close balance between excitation and damping.

ACKNOWLEDGEMENTS

We thank Wing-Kit Lee for helpful discussions and Tomoaki Matsumoto for comments on the manuscript. YL acknowledges NSF grant AST1352369.

REFERENCES

Amrein, W., Hinz, A., & Pearson, D. 2005, Sturm-Liouville Theory: Past and Present (Birkhäuser Basel)
Artymowicz, P., & Lubow, S. H. 1994, ApJ, 421, 651
Bate, M. R. 2000, MNRAS, 314, 33
Dempsey, A. M., Lee, W.-K., & Lithwick, Y. 2020a, ApJ, 891, 108
Dempsey, A. M., Muñoz, D., & Lithwick, Y. 2020b, ApJ, 892, L29
Duffell, P. C., & Chiang, E. 2015, ApJ, 812, 94

Duffell, P. C., D'Orazio, D., Derdzinski, A., et al. 2019, arXiv e-prints, arXiv:1911.05506
Dunhill, A. C., Cuadra, J., & Dougados, C. 2015, MNRAS, 448, 3545
Einstein, A. 1917, Verh. Deutsch. Phys. Ges., 19, 82
Farris, B. D., Duffell, P., MacFadyen, A. I., & Haiman, Z. 2014, ApJ, 783, 134
Frank, J., King, A., & Raine, D. J. 2002, Accretion Power in Astrophysics: Third Edition (Cambridge, UK: Cambridge University Press), 398
Goldreich, P., & Sari, R. 2003, ApJ, 585, 1024
Goldreich, P., & Tremaine, S. 1980, ApJ, 241, 425
Goodchild, S., & Ogilvie, G. 2006, MNRAS, 368, 1123
Gough, D. O. 2007, Astronomische Nachrichten, 328, 273
Ireland, M. J., & Kraus, A. L. 2008, ApJ, 678, L59
Keller, J. B. 1958, Annals of Physics, 4, 180
Kley, W., Papaloizou, J. C. B., & Ogilvie, G. I. 2008, A&A, 487, 671
Lanczos, C. 2012, Linear Differential Operators (Martino Publishing)
Landau, L., & Lifshitz, E. 1981, Quantum Mechanics: Non-Relativistic Theory, Course of Theoretical Physics (Elsevier Science)
Lee, W.-K., Dempsey, A. M., & Lithwick, Y. 2019a, ApJ, 872, 184
—. 2019b, ApJ, 882, L11
Liouville, J. 1837, Journal de Mathématiques Pures et Appliquées, 1
Lubow, S. H. 1991, ApJ, 381, 259
Lynden-Bell, D., & Ostriker, J. P. 1967, MNRAS, 136, 293
Lynden-Bell, D., & Pringle, J. E. 1974, MNRAS, 168, 603
MacFadyen, A. I., & Milosavljević, M. 2008, ApJ, 672, 83
Mardling, R. A. 2013, MNRAS, 435, 2187
Mark, J. W. K. 1977, ApJ, 212, 645
Miranda, R., & Lai, D. 2015, MNRAS, 452, 2396
Miranda, R., Muñoz, D. J., & Lai, D. 2017, MNRAS, 466, 1170
Miranda, R., & Rafikov, R. R. 2018, ApJ, 857, 135
Moody, M. S. L., Shi, J.-M., & Stone, J. M. 2019, ApJ, 875, 66
Moriwaki, K., & Nakagawa, Y. 2004, ApJ, 609, 1065
Muñoz, D. J., & Lai, D. 2016, ApJ, 827, 43
Muñoz, D. J., Lai, D., Kratter, K., & Miranda, R. 2020, ApJ, 889, 114
Muñoz, D. J., Miranda, R., & Lai, D. 2019, ApJ, 871, 84
Muñoz, D. J., Springel, V., Marcus, R., Vogelsberger, M., & Hernquist, L. 2013, MNRAS, 428, 254
Ogilvie, G. I. 2001, MNRAS, 325, 231
—. 2007, MNRAS, 374, 131
—. 2008, MNRAS, 388, 1372
Paardekooper, S. J., Thébault, P., & Mellema, G. 2008, MNRAS, 386, 973
Pakmor, R., Springel, V., Bauer, A., et al. 2016, MNRAS, 455, 1134
Papaloizou, J. C. B. 2002, A&A, 388, 615
Popham, R., & Narayan, R. 1991, ApJ, 370, 604
Price, D. J., Cuello, N., Pinte, C., et al. 2018, MNRAS, 481, 3169
Pryce, J. 1993, Numerical Solution of Sturm-Liouville Problems, Monographs on numerical analysis (Clarendon Press)
Rafikov, R. R. 2016, ApJ, 827, 111
Regály, Z., Sándor, Z., Dullemond, C. P., & Kiss, L. L. 2011, A&A, 528, A93
Roedig, C., Dotti, M., Sesana, A., Cuadra, J., & Colpi, M. 2011, MNRAS, 415, 3033
Shi, J.-M., Krolik, J. H., Lubow, S. H., & Hawley, J. F. 2012, ApJ, 749, 118
Shu, F. H., Tremaine, S., Adams, F. C., & Ruden, S. P. 1990, ApJ, 358, 495
Silsbee, K., & Rafikov, R. R. 2015, ApJ, 808, 58
Simon, B. 1976, Annals of Physics, 97, 279
Springel, V. 2010, MNRAS, 401, 791
Statler, T. S. 2001, AJ, 122, 2257
Teyssandier, J., & Ogilvie, G. I. 2016, MNRAS, 458, 3221
—. 2017, MNRAS, 467, 4577
Thun, D., Kley, W., & Picogna, G. 2017, A&A, 604, A102
Tiede, C., Zrake, J., MacFadyen, A., & Haiman, Z. 2020, ApJ, 900, 43
Tofflemire, B. M., Mathieu, R. D., Ardila, D. R., et al. 2017, ApJ, 835, 8
Tofflemire, B. M., Mathieu, R. D., & Johns-Krull, C. M. 2019, AJ, 158, 245
Tremaine, S. 2001, AJ, 121, 1776
Whitehurst, R. 1994, MNRAS, 266, 35

APPENDIX

HIGHER ORDER EIGENMODES

When $h_0 \lesssim 0.05$, the quantization condition (11) can be satisfied by more than one frequency. This new behavior is illustrated in Figure 11, which shows that the function $\omega_{\rm pot}$ (in units of $\frac{1}{2}h_0^2\Omega_{\rm b}$, left panel) is taller and wider than that shown in Figure 5 for when h_0 is reduced from 0.1 to 0.03. This corresponds to changing $\omega_{\mathcal{P}}/\omega_{\mathcal{Q}}$ from 0.33 to 0.03. This effective potential now allows for two trapped modes, as highlighted by the closed contours of the DRM (middle panel). A numerical solution of the BVP (right panel) shows that a lower frequency one-node mode can accompany the fundamental mode.

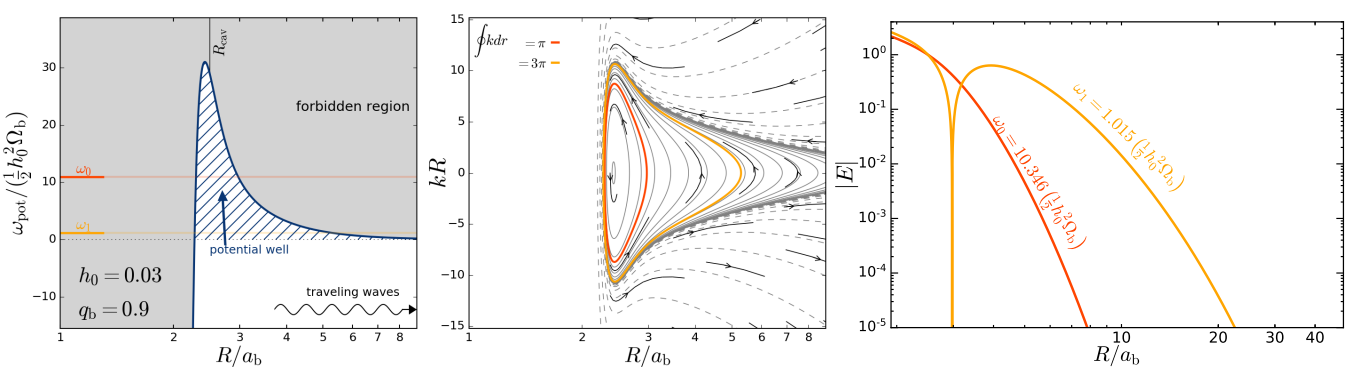

Figure 11. Left and middle panels: similar to Figure 5, but for $h_0 = 0.03$, which allows for the existence of a fundamental mode ($n = 0$, red) and a first harmonic ($n = 1$, orange) to be trapped. Right panel: eigenfunctions associated to the $n = 0$ (red) and $n = 1$ (orange) modes; the first harmonic contains a node at $R \approx 3a_{\rm b}$ and its frequency ω_1 is 10 times lower than that of the fundamental mode ω_0.

QUANTUM HARMONIC OSCILLATOR

In the vicinity of $\xi = \xi_{\rm peak}$, the term in square brackets in Equation (9) can be expanded to quadratic order in ξ, simplifying the eccentricity equation to

$$\frac{9\omega_{\mathcal{P}}}{32}\frac{d^2Y}{d\xi^2} + \left[25\omega_{\mathcal{P}} + 1.13\omega_{\mathcal{Q}} + 260\omega_{\mathcal{P}}(\xi-\xi_{\rm peak}) - 15000\omega_{\mathcal{P}}(\xi-\xi_{\rm peak})^2\right]Y = \omega Y\ , \tag{B1}$$

which is of the generic form

$$\hat{H}Y \equiv \left[\frac{A}{2}\frac{d^2}{d\xi^2} + B + C(\xi-\xi_0) - \frac{D}{2}(\xi-\xi_0)^2\right]\psi = \omega Y\ . \tag{B2}$$

If we transform the independent coordinate to $x = \left(D/A\right)^{1/4}\left(\xi - \xi_0 - \frac{C}{D}\right)$, Equation (B2) can be cast into a quantum harmonic oscillator (QHO) form

$$\left[-\frac{1}{2}\frac{d^2}{dx^2} + \frac{x^2}{2}\right] Y = (AD)^{-1/2}\left[\frac{C^2}{2D} + B - \omega\right] Y \equiv \tilde{\omega} Y \ , \tag{B3}$$

which has exact eigenfrequencies $\tilde{\omega}_n = n + 1/2$, and thus the operator $\hat{H}$ in Equation (B2) has eigenvalues

$$\omega_n^{\rm QHO} = -\sqrt{AD}\left(n + \frac{1}{2}\right) + \frac{C^2}{2D} + B \ . \tag{B4}$$

Since $A = (9/16)\omega_{\mathcal{P}}$, $B \approx 25\omega_{\mathcal{P}} + 1.13\omega_{\mathcal{Q}}$, $C \approx 260\omega_{\mathcal{P}}$ and $D = 3\times 10^4\omega_{\mathcal{P}}$, the eccentricity eigenvalues can be approximated by

$$\omega_n^{\rm QHO} = 1.13\omega_{\mathcal{Q}} + 26.1\omega_{\mathcal{P}} - 130\omega_{\mathcal{P}}\left(n + \frac{1}{2}\right) \ . \tag{B5}$$

APPROXIMATED QUANTIZATION CONDITION

The quantization condition (11) between two turning points, $R_{\rm tp,1}$ (left) and $R_{\rm tp,2}$ (right), cannot be solved analytically for ω_0. However, an approximate expression can be obtained if we make three assumptions: (*i*) that the modes are shallow (i.e., that $\omega_0 \ll \max[\omega_{\rm pot}]$), (*ii*) that $R_{\rm tp,1}$ is the same for all eigenmodes due to the steep decline of $\omega_{\rm pot}$, and (*iii*) that, at the right turning point where $\omega_0 = \omega_{\rm pot}$, the disk is approximately a power-law and $\omega_{\rm pot} \approx \Omega f_0$. Then, we approximate Equation (11) with

$$(kR)_{\rm max}\Delta \ln R \sim \pi \tag{C1}$$

where $\Delta \ln R \simeq \ln(R_{\rm tp,2}/R_{\rm tp,1})$, and where assumption (*iii*) implies that the right turning point satisfies $R_{\rm tp,2} \approx R_{\rm cav}(\omega_0/\omega_{\mathcal{Q}})^{-2/7}$. Since the modes are shallow, $kR \simeq (R/R_{\rm cav})^{3/4}(2\omega_{\rm pot}/\omega_{\mathcal{P}})^{1/2}$ (Equation 7) and thus, in order to solve Equation (C1) for ω_0, we just need to know $\max[(R/R_{\rm cav})^{3/4}(2\omega_{\rm pot}/\omega_{\mathcal{P}})^{1/2}]$. If $C_{\mathcal{P}}\omega_{\mathcal{P}}$ is the local maximum of the pressure contribution to $\omega_{\rm pot}$, then we can rearrange the effective potential as $\omega_{\rm pot} = C_{\mathcal{P}}\omega_{\mathcal{P}}\left[V_{\rm press}(x) + \epsilon x^{-7/2}\right]$, where dimensionless function $V_{\rm press}$ evaluates to 1 at $x \equiv R/R_{\rm cav} \simeq 1$, and where we have defined $\epsilon \equiv \omega_{\mathcal{Q}}/(C_{\mathcal{P}}\omega_{\mathcal{P}})$ which is small for all of the simulations carried out in this work. Thus, if we replace $(kR)_{\rm max}$ with $\sqrt{2C_{\mathcal{P}}}(1+\epsilon/2)$ and $\Delta \ln R$ with $\ln[(R_{\rm cav}/R_{\rm tp,1})(\omega_0/\omega_{\mathcal{Q}})^{-2/7}]$ in Equation (C1), then we can solve for ω_0. We empirically find, for our assumed Σ profile, that $2C_{\mathcal{P}} \simeq 50$ and $R_{\rm tp,1} \simeq 0.92R_{\rm cav}$, and therefore we have

$$\omega_0 \sim {\rm e}^{-1.28+\pi\frac{\epsilon}{4}}\ \omega_{\mathcal{Q}} \ . \tag{C2}$$

Therefore, the mode tapering radius (Equation 13) is, to first order in ϵ,

$$\lambda = R_{\rm cav}\left(\frac{9}{32}\frac{\omega_{\mathcal{P}}}{\omega_0}\right)^{2/3} \sim R_{\rm cav}\left(\frac{\omega_{\mathcal{P}}}{\omega_{\mathcal{Q}}}\right)^{2/3}\left[1 - 0.02\frac{\omega_{\mathcal{Q}}}{\omega_{\mathcal{P}}}\right] \ . \tag{C3}$$